Fluid–structure coupling in time domain for dynamic stall using purely Lagrangian vortex method

Article *in* CEAS Aeronautical Journal · April 2021

DOI: 10.1007/s13272-021-00511-z

3 authors:

Duong Viet Dung
Vietnam National University, Hanoi
12 PUBLICATIONS **10** CITATIONS
SEE PROFILE

Lavi Rizki Zuhal
Bandung Institute of Technology
48 PUBLICATIONS **193** CITATIONS
SEE PROFILE

Hari Muhammad
Bandung Institute of Technology
30 PUBLICATIONS **49** CITATIONS
SEE PROFILE

CEAS Aeronautical Journal
https://doi.org/10.1007/s13272-021-00511-z

ORIGINAL PAPER

Fluid–structure coupling in time domain for dynamic stall using purely Lagrangian vortex method

Viet Dung Duong[1] · **Lavi Rizki Zuhal**[2] · **Hari Muhammad**[2]

Received: 10 August 2020 / Revised: 14 March 2021 / Accepted: 31 March 2021

Abstract
This paper presents the purely fast Lagrangian vortex method (FLVM) for the simulation of the external incompressible flows past heaving and pitching bodies with high-frequency oscillation. The Nascent vortex element is introduced to the flow field to retain the Lagrangian characteristics of the solver. The viscous effect is modeled using a core spreading method coupled with the splitting and merging spatial adaptation scheme. The particle's velocity is calculated using Biot–Savart formulation. To accelerate computation, a fast multipole method (FMM) is employed. The validity of FLVM solver is verified by temporal and spatial convergence studies for the case of flows past an impulsively started cylinder at the Reynolds numbers ranging from 50 to 9500. The accuracy of FLVM is then confirmed for the simulation of flows around the pitching flat plate and oscillating airfoil. The time history of drag and lift coefficients and the vorticity contours show a good agreement with those reported in literature. Furthermore, the FLVM is employed to determine the flutter derivatives and flutter speed of an oscillating flat plate. Results are compared with theoretical solutions based on Theodorsen's function. In general, the results agree well with those obtained by the inviscid theory.

Keywords Vortex particle method · Core spreading method · Viscous flow · Flutter derivatives · Flutter speed · High frequency oscillation

1 Introduction

Fluid structure interaction of engineering structures is where fluid flow exerts pressure on a solid structure causing it to collapse such that it perturbs the initial fluid flow. This type of interaction causes the aeroelastic instability phenomenon due to self-induced forces. In addition, the aeroelastic instability, which introduces the structural flutter, leads to large vibration amplitudes of structures. Eventually, the flutter instability collapses the structures totally, see Scanlan and Tomo [1]. Hence, the comprehensive understanding of flutter instability plays an essentially important role to determine a standard criterion for the engineering designs and similarly to other criterions related to effects of dead load, live load, and possibly earthquake.

Recently, wind tunnel testing was frequently used to determine the flutter stability of bridges [1–3]. Section model tests have shown to be an inexpensive, reliable, and robust experimental tool. Nevertheless, various computational fluid dynamics (CFD) methods have been developed in recent years to contribute alternative features along with tremendous development of the computing power and speed. That is because the better understanding of vortical flow structures is improved by numerical tools of flow visualization. In addition, the economic cost can be cut off by substituting the wind tunnel testing by numerical calculations in the preliminary stage of aerodynamic designs. Edward and William [4] applied a potential theory based on a doublet-lattice method to compute lift coefficients on oscillating surfaces under subsonic flow configuration. The lifting surfaces are linearized and idealized as a set of lifting panels in which the approximate solutions are obtained.

✉ Viet Dung Duong
duongdv@vnu.edu.vn

Lavi Rizki Zuhal
lavirz@ae.itb.ac.id

Hari Muhammad
hari@ftmd.ac.id

[1] School of Aerospace Engineering, University of Engineering and Technology, Vietnam National University, Ha Noi City, Vietnam

[2] Faculty of Mechanical and Aerospace Engineering, Institut Teknologi Bandung, Bandung, Indonesia

Published online: 11 April 2021

Edwards et al. [5] investigated the angle-of-attack effects on the time-matching flutter solutions of plunging and pitching airfoils in transonic flow conditions using a complex model identification technique based on an exponential function. The determination of flutter boundaries with respect to angle of attack and Mach number was reported with the elimination of leading edge shocks. The multiple flutter speeds at a given mach number were found due to the existence of static pitching moments. Alonso and Jameson [6] extracted the aeroelastic solutions using a fully implicit time matching algorithm for transonic flow applications. The multigrid methods were integrated with the implicit Euler equations and a first-order decomposition of the structural equations. The flutter boundaries were reported to be consistent with existing numerical data. Prananta et al. [7] considered the viscous transonic flow simulation using an robust efficient algorithm based on implicit time matching for the solutions of two-dimensional unsteady thin-layer Navier–Stokes equations to carry out the aeroelastic analysis of a two-degree-of-freedom airfoil. Hall et al. [8] applied proper orthogonal decomposition (POD) technique to build the reduced-order model (ROM) of unsteady disturbance for turbulent transonic flows. The unsteady aerodynamic and aeroelastic solutions of a single airfoil and a two-dimensional cascade of airfoils were numerically investigated using the POD/ROM algorithm. Bohbot et al. [9] computed the flutter boundary of two-degree-of-freedom transonic airfoil using a parallel time-matching nonlinear flow solver combined with a structure solver. The flutter boundary accuracy was obtained with three hundred runs using a parallel implicit algorithm. The shock wave effects on the airfoil motion, damping effects due to flow viscosity on flutter and Hopf bifurcations were reported by the solver with the employment of Spalart–Allmaras turbulence model.

Tang and Dowell [10] experimentally and theoretically studied the aeroelastic response of high aspect ratio wing models due to flutter and limit-cycle oscillations obtained by wind tunnel test. The flutter velocity and oscillation frequency were determined by a dynamic perturbation analysis related to nonlinear static equilibrium. The theoretical results were made to resurrect the experiment data. Liu et al. [11] integrated a unsteady, parallel, multiblock, and multigrid computational fluid dynamics solver with structural dynamics method for prediction and simulation of flutter. The structural dynamics method employed the time integration of modal dynamic equations, which are extracted from finite element analysis. The aeroelastic system was directly investigated from the time domain for the determination of aeroelastic system stability using the indicial response as input. Meanwhile the solutions of the flutter boundary via the flutter equation were computed in frequency domain. The two- and three-dimensional wing aeroelastic models were simultaneously performed to compare with experimental data. Chen et al. [12] developed a finite volume method coupled with a Roe moving grid scheme for the fluid–structure interaction to predict the airfoil flutter under the transonic flow configuration. The linear structural equations were implicitly combined through pseudo time stepping with sequential iteration. The moving and deformation mesh is clarified by fine mesh zone without deformation and coarse mesh zone deformed with solid object's deformation. The flutter boundary of elastic airfoil was then computed along with aerodynamic coefficients under both the steady state flow and limit cycle oscillation (LCO) conditions.

Badcock et al. [13] investigated the direct aeroelastic bifurcation analysis of a three-dimensional symmetric flexible AGARD 445.6 wing in inviscid transonic flow configuration using a sparse matrix solver on the solution of Euler equations. The determination of the entire flutter boundary of the wing was clarified in a time domain. Badcock and Woodgate [14] developed a framework based on the combination of computational fluid dynamics and finite element solvers to produce highly accurate results in practical applications with the support of parallelization algorithms. The bifurcation prediction of aeroelastic models of three-dimensional wing and full aircraft models was investigated to confirm the performance of coupling solvers. Badcock et al. [15] investigated the aeroelastic numerical models with very large dimensions using a computational fluid dynamics solver. The full aircraft model was performed to discover the nonlinear reduced order models for the computation of limit cycle responses. Timme et al. [16] employed Kriging-assisted Schur complement formulation to determine the aeroelastic stability and optimization of full aircraft models in transonic flow configuration. The numerical results were assisted by a Kriging extrapolation to cover the parameter space. The kriging-based multiobjective optimization of transport wing designated stability analyses for whole flight envelopes. Wang et al. [17] numerically applied mesh adaptation scheme based on adjoint variables for direct flutter prediction in supersonic flow configuration. The elastic structure was modeled using von Karman plate theory while the fluid pressure was modeled by potential flow theory with the employment of mesh feature-based adaptation scheme.

For the practical applications, at the sufficient high flow speeds, flutter instability causes the structure undergoing a simple harmonic motion. Otherwise, the forces, developed due to a bluff or streamlined bodies undergoing time-dependent motion in a steady fluid flow, will also be harmonic with high frequency. Hence, to predict the flutter instability, the aerodynamic coefficients of the flutter instability (flutter derivatives) are to be evaluated to model the harmonic fluid forces by prescribing the motion of a streamlined body to be purely translational or purely rotational. Otherwise, the critical flutter speed of the streamlined bodies is calculated based on the computed flutter derivatives. Hence, the output

of the critical flutter speed will be an essential parameter for the engineering designs. Apart from the flutter determination methods extensively reviewed above, the numerical methods are classified into grid-based methods (finite element method [18], finite volume method [19]) and vortex particle methods [20, 21] to determine the aerodynamic coefficients. The vortex particle methods are more advantageous than the grid-based methods due to its meshfree characteristics, which refuses the grid adaptation for the case of flows past a structure under harmonic motions. Koumoutsakos and Leonard [22] elaborated an analytical solution, based on vortex sheet diffusion induced by vortex panels at solid walls, for satisfaction of no-slip boundary condition in vortex methods. The vortex sheet scheme was proved to be stable for the wide range of Reynolds numbers from 40 to 9500. Ploumhans and Winckelmans [23] developed grid-free particle strength exchange (PSE) scheme for diffusion in the cases of bounded flow simulations. For the convection, the velocity computation was accelerated using the fast multipole method. To support the high-resolution simulations to disregard the particle distortion, the M'_4 interpolation scheme, which is a grid-based approach, was utilized. Ploumhans et al. [24] further extended the particle strength exchange scheme and vortex sheet algorithm for high-resolution simulation of three-dimensional unsteady incompressible flows past complex geometries. The grid-based non-uniform resolution, namely the redistribution lattice mapping, was employed to support the use of parallel tree codes in the context of multipole expansions of vortex particles and of vortex panels. Kamemoto [25] advanced a purely Lagrangian vortex method for the practical engineering flow simulations in two- and three-dimensional incompressible fluids. The no-through and no-slip boundary conditions for complex geometries were considered using a boundary element method and introduction of Nascent vortex elements from wall panels, respectively. However, the Lagrangian error due to the particle distortion was not treated in the case of high Reynolds number. Cottet and Poncet [26] elaborated an advance in direct numerical simulation using particle-in-cell method for three-dimensional incompressible wall-bounded flows. The immersed boundary method was carried out for the complex geometries. The particle-in-cell and immersed boundary methods were employed to be grid-based approaches for the acceleration of velocity computation and no-slip boundary condition of wall-bounded geometries, respectively. Yokota et al. [27] utilized the purely Lagrangian core spreading vortex method for three-dimensional simulation of decaying homogeneous isotropic turbulence flows without the presence of a solid wall. A fast multipole method was implemented for periodic boundary conditions. The meshfree spatial adaptation scheme based on radial basis function technique was executed for the consideration of particle distortion. Walther and Morgenthal [28] implemented the immersed interface technique based on a boundary element method for the flow simulation of complex geometries. The particle–mesh hybrid method was employed using a vortex-in-cell method to resolve the smallest vortex scales due to the existence of the immersed interface and to ignore the overlapping issue of Lagrangian particles. Huang et al. [29] resurrected the purely Lagrangian vortex method by employing meshfree core spreading technique and vortex sheet diffusion for diffusion process and no-slip boundary conditions, respectively. The core spreading particles were revitalized by splitting and merging adaptation schemes to get rid of Lagrangian error due to particle overlapping issues. Huang et al. [30] continuously extended the core spreading vortex method for long time flow simulation of arbitrary geometries. Although the capability of the method enables the flow simulations of the complex geometries, the complex dynamic motions of the geometries, which are essential for practical engineering applications, were not considered. Hammer et al. [31] validated the discrete vortex method based on thin airfoil theory for the low Reynolds number unsteady incompressible flow simulations. The no-through and no-slip boundary conditions were satisfied and the solver supports the rapid computation of flowfield and force coefficients in unsteady aerodynamic applications. However, the model of boundary layer was not elaborated in the case of low Reynolds number. Mimeau et al. [32] applied a continuous forcing immersed boundary method, namely vortex penalization method, for the direct numerical simulations of flows past obstacles in three-dimensional incompressible fluids. The FFT-based Poisson solver was utilized for the far field boundary conditions. The penalization method is a grid-based approach to deal with the complex geometries in a complex flow configuration.

The present work that follows relies on fully resolved direct numerical simulations using a purely fast Lagrangian vortex method (FLVM) [33, 34]. Specifically, the developed method simulates the external flows around complex geometry by tracking freely local velocities and vorticities of particles introduced within the fluid domain. The Nascent vortex element is introduced to the flow field to retain the purely Lagrangian characteristics of the solver. The viscous effect is modeled using a core spreading method coupled with the splitting and merging spatial adaptation scheme to resolve the boundary layer induced by solid walls. The particle's velocity is calculated using Biot–Savart formulation. To accelerate computation, a fast multipole method (FMM) is employed. Accordingly, the FLVM solver produces the aerodynamic forces as an input to determine structural characteristics. The quality of calculations using the solver does not only depend on the quality of the meshfree solver but also to enable its great extent on the modeling of flutter instability. Hence, the originality of this work is to extend the capability of FLVM computational fluid dynamics to

the determination of high frequency structural oscillation and aeroelastic instability of structures. In particular, the present paper extracts desired aerodynamic data from the FLVM solver and demonstrates their importance to aeroelastic analysis in engineering applications. Numerical solver validation, flow simulations, and discussions of the results will be given with reference listed in literature. The rest of this paper is organized as follows: Sect. 2 expresses the governing equations and numerical method of FLVM, Sect. 3 describes the structural analysis solver for the flutter determination, Sect. 4 gives computational setup, Sect. 5 produces the discussions on results, followed by the conclusions in Sect. 6.

2 Lagrangian vortex method

The vortex methods are based on the momentum equation and the continuity equation for incompressible flow which are written in vector form as follows:

$$\frac{\partial \underline{u}}{\partial t} + \left(\underline{u} \cdot \nabla\right)\underline{u} = -\frac{1}{\rho}\nabla p + \nu \nabla^2 \underline{u} \tag{1}$$

$$\nabla \cdot \underline{u} = 0 \tag{2}$$

Taking the curl and divergence operators of Eq. (1) and simplify using (2), these equations become:

$$\frac{\partial \underline{\omega}}{\partial t} + \left(\underline{u} \cdot \nabla\right)\underline{\omega} = \left(\underline{\omega} \cdot \nabla\right)\underline{u} + \upsilon \nabla^2 \underline{\omega}, \tag{3}$$

$$\nabla^2 p = -\rho \nabla \cdot \left(\underline{u} \nabla \underline{u}\right), \tag{4}$$

where $\underline{u}$ is velocity vector, p the pressure, υ the kinematic viscosity, and ρ the density. The vorticity $\underline{\omega}$ is defined as

$$\underline{\omega} = \nabla \times \underline{u}. \tag{5}$$

The pressure p can be independently calculated by the Poisson Eq. (4) once needed. Lagrangian expression for the vorticity transport expressed in Eq. (3) is then given by

$$\frac{\mathrm{d}\underline{\omega}}{\mathrm{d}t} = \left(\underline{\omega}.\nabla\right)\underline{u} + \nu \nabla^2 \underline{\omega}. \tag{6}$$

When a two-dimensional flow is dealt with, the stretching term, which is the first term on the right hand side of Eq. (6), disappears and the two-dimensional vorticity transport equation is simply reduced to diffusion equation:

$$\frac{\mathrm{d}\underline{\omega}}{\mathrm{d}t} = \nu \nabla^2 \underline{\omega}. \tag{7}$$

This equation is solved numerically, using a viscous splitting algorithm. The algorithm includes convection and diffusion steps. In the convection step, the particles containing the local velocity and vorticity are freely advected by the following equation,

$$\frac{\mathrm{d}\underline{x}}{\mathrm{d}t} = \underline{u}\left(\underline{x}, t\right). \tag{8}$$

With their own local convective velocities using Biot–Savart formulation

$$\underline{u}\left(\underline{x}, t\right) = \frac{1}{2\pi} \int \frac{\underline{\omega}\left(\underline{x}', t\right) \times \left(\underline{x} - \underline{x}'\right)}{\left|\underline{x} - \underline{x}'\right|^3} \mathrm{d}\underline{x}' \tag{9}$$

where $\underline{x}$ is the position vector. The term inside integral in Eq. (9) is integrated over all particles within the computational domain. The Biot–Savart formulation is called N-body problem that involves $O\left(N^2\right)$ evaluations, which directly compute the particle's velocity. It makes this method not practical due to high cost and expensive memory requirements. To deal with this issue, the fast multipole method is employed to reduce the $O\left(N^2\right)$ to $O(N\log N)$ operations, as discussed in more details in the following section. Equation (8) is solved using the fourth-order Runge–Kutta method:

$$\underline{x}^{n+1} = \underline{x}^n + \frac{\Delta t}{6}\left(\underline{u}\left(\underline{x}^n\right) + 2\underline{u}\left(\underline{x}_1\right) + 2\underline{u}\left(\underline{x}_2\right) + \underline{u}\left(\underline{x}_3\right)\right), \tag{10}$$

where Δt is the time step, and $\underline{u}\left(\underline{x}^n\right)$, $\underline{u}\left(\underline{x}_1\right)$, $\underline{u}\left(\underline{x}_2\right)$, $\underline{u}\left(\underline{x}_3\right)$ are the particle velocities at $\underline{x}^n$ (the particle position at time step n), $\underline{x}_1$, $\underline{x}_2$, and $\underline{x}_3$. The particle locations $\underline{x}_1$, $\underline{x}_2$, and $\underline{x}_3$ are obtained as follows:

$$\underline{x}_1 = \underline{x}^n + \underline{u}\left(\underline{x}^n\right)\frac{\Delta t}{2}, \tag{11}$$

$$\underline{x}_2 = \underline{x}^n + \underline{u}\left(\underline{x}_1\right)\frac{\Delta t}{2}, \tag{12}$$

$$\underline{x}_3 = \underline{x}^n + \underline{u}\left(\underline{x}_2\right)\Delta t. \tag{13}$$

In the diffusion step, the diffusion term $\nu \nabla^2 \underline{\omega}$ is evolved by spreading the core size of particles in time, which is further discussed in the following section.

2.1 Vortex convection with fast multipole method

To overcome the N-body problem mentioned above, the fast multipole method (FMM) is employed in this work to accelerate the velocity computation following the works of Greengard and Rokhlin [35] and Hrycak and Rokhlin [36].

The method significantly reduces the velocity computation time due to the fact that interactions among particles are not computed directly. In particular, the FMM employs the regularized equation for direct calculation in the short-range interaction, meanwhile the far-range interaction is still considered via singular distributing function and approximated using the derived multipole and local expansions. The implementation of multipole and local expansions for approximating the singular distribution equation is used to accelerate the regularized equation.

In more details, as depicted in Fig. 1, the FMM initially constructs the data of particles by tree structure of the box in which particles are laid on, as shown in Fig. 1a,b. Afterwards, the direct interactions of box's centers are evaluated using multipole expansion of all these centers, as demonstrated in Fig. 1c. Eventually, the interaction of all direct particle pairs is translated from these centers to their own particles via local expansion. Basically, the multipole expansion is generated by particles inside the circle of radius R and converged outside the box. The local expansion is generated by particles outside the circle of radius R and converged within the box. The multipole and local expansions can be referred in more details in [35, 36]. Therefore, it reduces huge amount of computation process from $O(N^2)$ to $O(N\log N)$.

Figure 2 shows the computational acceleration achieved using FMM with 250 and 500 boxes arranged in adaptive quad-tree structures. In the figure, computational time using the direct Biot–Savart (Eq. 9) and FMM is plotted against the number of particles used during a simulation. As can be seen, the difference in the computational time between the two methods is small up to around 120,000 particles.

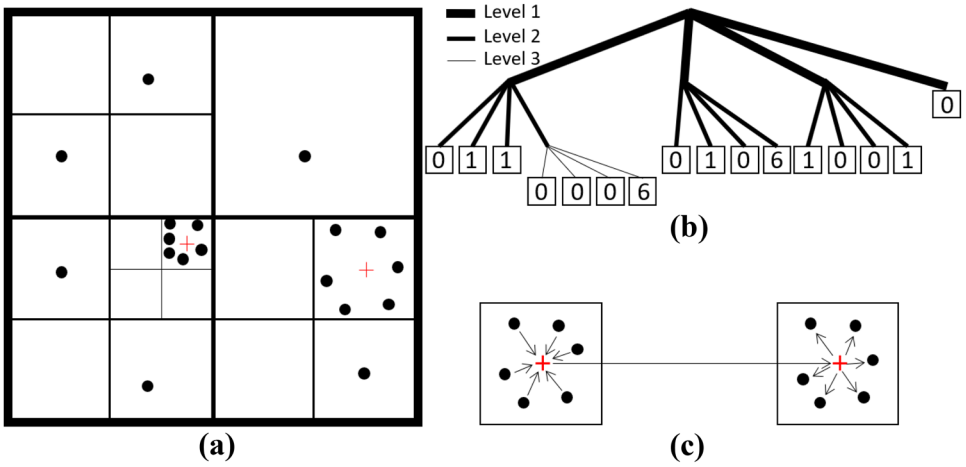

Fig. 1 FMM concept. **a** 2-D domain clustering: adaptive quad-tree structure; **b** tree structure for the storage of a particle cluster; **c** local and multipole expansions

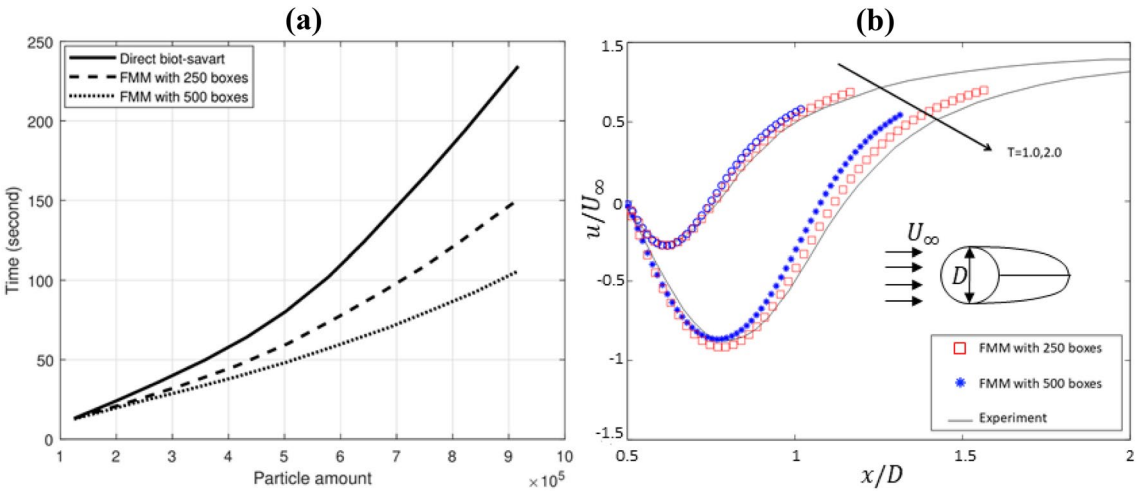

Fig. 2 **a** Comparison between direct Biot–Savart and FMM computational time. **b** Effect of initial amount of FMM tree boxes on the velocity computation in the case of impulsively started cylinder at $Re = 550$. The *square-dashed line* is the present result with 250 boxes of FMM trees. The *asterisk-dashed line* is the present result with 500 boxes of FMM trees. The *continuous line* is the experimental data by Buard and Coutanceau [37]

However, the FMM-based velocity acceleration increases drastically as the number of particles increases beyond 700,000. The more adaptive quad-tree box amount supports the more speedup of velocity computation. For the convergence of the flow field computation, Fig. 2b depicts the effect of initial amount of FMM tree boxes on the velocity computation in the case of impulsively started cylinder at $Re = 550$. As shown in the figure, the more operations of multipole and local expansions produces the higher deviation of velocity results with those listed in literature. Consequently, the employment of FMM essentially allows longer simulation time, which is found in practical applications.

2.2 Vortex diffusion with adaptation schemes

In the diffusion step, the diffusion term $\nu\nabla^2\underline{\omega}$ in the right-hand side of diffusion Eq. (7) is evolved by spreading core size of particle ($\sigma_p(t) = \sqrt{4\nu\Delta t}$) in time as follows

$$\frac{d\sigma_i}{dt} = \frac{2\nu}{\sigma_i}. \tag{14}$$

The total numerical truncation error, the Lagrangian effect noticed by Greengard [38], is introduced in solving the Eq. (14). This error increases proportionally with the spreading rate of change of particle core size. Increasing the core size of each particle makes the particle advect with its average velocity, rather than its local velocity. Hence, there is a need for a spatial adaptation scheme to control the core size of the particle to be small enough to minimize the Lagrangian effect and maintain the spatial resolution. To deal with the Lagrangian effect after spreading the core size of particles in time in Eq. (14), Rossi [39] proposed the splitting scheme to spatially adapt the flow field. In particular, if the core radius of the vortex blob is larger than a threshold, then the parent blob is split into the several smaller children blobs, and the vortex strengths of the parent blobs are divided by the number of the children. Then, the children's core radius is reset into the smaller core radius.

The threshold core size, σ_{max}, is chosen to be $\sqrt{6}\sigma$ to sufficiently control the particle distribution over time. On the other hand, as long as core size σ_j is larger than the threshold σ_{max}, the particle with core size σ_j would be split into a set of thinner core particles, where each particle inside the set has core size equal to $\alpha\sigma_j$. This set also satisfies the zero, the first moments of vorticity as follow:

$$\Gamma_p = \sum_{c=1}^{M} \Gamma_c, \tag{15}$$

$$\Gamma_p \underline{x}_p = \sum_{c=1}^{M} \Gamma_c \underline{x}_c, \tag{16}$$

where Γ_p, Γ_c stand for vorticity strengths of parent particles before splitting event, and children particles after splitting event. M is the number of child particles. M is observed to be equal to 5 during our simulation for the high-resolution results as depicted in Fig. 3. The free parameter r is given by

$$r = \sigma_j\sqrt{2\left(1-\alpha^2\right)}, \tag{17}$$

where α is overlapping parameter and set to be equal to 0.85. As a result, the children's cores are overlapped after several splitting events and the splitting scheme eventually introduces the large amount of vortex elements, which is larger than the required vortex elements to sufficiently resolve the flow. Thus, the merging scheme is also proposed for the particle population control and the overlapping control. The merging scheme is followed by the works of Huang et al. [29], and Dung et al. [33].

Figure 4 illustrates the merging adaptation scheme. The particles, represented by the red circles, are formed after the merging process. The black dots stand for the unmerging particles. In this scheme, if $\left(\underline{x}_j, \Gamma_j, \sigma_j, j = 1, \ldots N\right)$ are the set of nearby particles, then those nearby particles are going to be replaced by one $\underline{x}_0, \Gamma_0, \sigma_0$ such that

$$\Gamma_0 = \sum_{j=1}^{N} \Gamma_j, \tag{18}$$

$$\Gamma_0 \underline{x}_0 = \sum_{j=1}^{N} \Gamma_j \underline{x}_j, \tag{19}$$

$$\Gamma_0\sigma_0 = \sum_{j=1}^{N} \Gamma_0\left(\sigma_0^2 + \left|\underline{x}_0 - \underline{x}_j\right|^2\right). \tag{20}$$

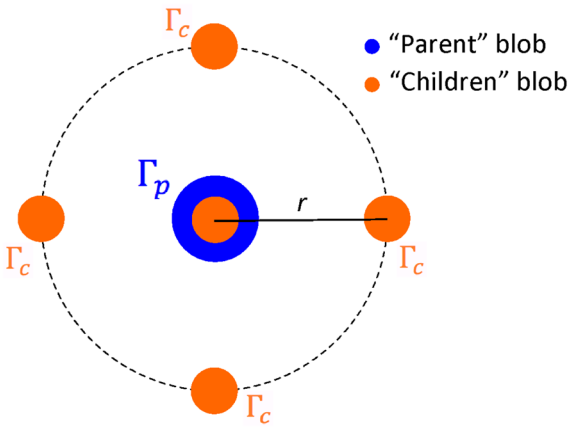

Fig. 3 Spitting scheme for a parent particle

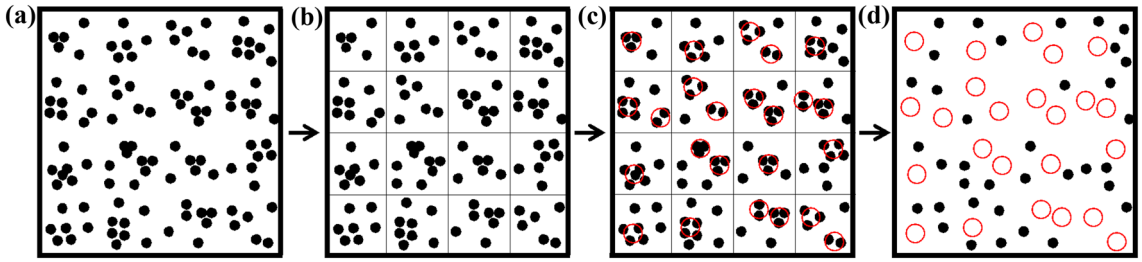

Fig. 4 Illustration of merging scheme. The particles, represented by the *red circles*, are formed after the merging process. The *black dots* stand for the unmerging particles

Meanwhile following thresholds should be satisfied

$$\Gamma_0 < \Gamma_{\text{ref}} \varepsilon \alpha^2 \alpha_{\max}^2, \tag{21}$$

$$\sigma_0 < \sigma_{\max}, \tag{22}$$

where Γ_{ref} and ε are the reference vorticity strength, and the error tolerance, respectively. In further details, the merging scheme in the figure is algorithmically expressed step by step as follows.

1. Find the region that will be occupied by all the computational elements as shown in Fig. 4a.
2. Divide the region into rectangular cells ($\Delta x = \Delta y = 0.5\sigma$) and select elements within each cell and form a set of particle $\left(\Gamma_i, x_i, \sigma_i\right)_{i=1}^{m}$, where m is the number of particles in the cell, as shown in Fig. 4b.
3. Renumber the elements successively from one cell to another. For instance, a cell c has m particles.
4. As shown in Fig. 4c, for each cell in which there exists more than one element, do the following loop:
   a. Consider the neighbors of particle $i (i = 1, \ldots, m)$.
   b. If thresholds (21) and (22) are both satisfied, then keep the merging process by solving the Eqs. (18), (19) and (20) to get the new merging particle $\left(\Gamma_0, x_0, \sigma_0\right)$.
   c. Renew the merging particle and remove the particle i together with its neighbors.
   d. If one of these thresholds is not satisfied, then break the loop.

The merging process is completed after step 4. The population of particles, shown in Fig. 4d after the merging process, is reduced and the spatial resolution is maintained.

2.3 No-through and no-slip boundary conditions

Bounded flow problems require the enforcement of the no-through and no-slip conditions on boundary. In the present FLVM, the no-through enforcement is accomplished through the use of boundary element methods (BEM), which was utilized by Walther and Morgenthal [28]. The BEM calculates a vortex sheet's strength $\underline{\Gamma}$, which represents the slip velocity on the boundary to satisfy no-through condition. In BEM, the boundary, S is discretized into panels and the vortex strength of each panel is calculated. These vortex strengths represent initial vorticity vectors on the wall panels. The calculated vortex strength is a vector with wall-tangent component, $\hat{t}$, and a normal component, $\hat{n}$, which satisfied the no-through condition. In the computation of vortex panel distribution, the Fredholm integral of second kind is employed as

$$\underline{u}_{\text{slip}} \cdot \hat{t} = \frac{\underline{\Gamma}\left(\underline{x}'\right) \times \hat{n}}{2} + \int_S \underline{\Gamma}\left(\underline{x}'\right) \times \nabla G\left(\underline{x} - \underline{x}'\right) \cdot \hat{t}\left(\underline{x}\right) \mathrm{d}s\left(\underline{x}'\right). \tag{23}$$

where $\underline{u}_{\text{slip}}$ is spurious slip velocity on the wall that is obtained after convection and diffusion steps. $G\left(\underline{x} - \underline{x}'\right)$ stands for Green function. The Eq. (23) enables the direct computation of vortex panel distribution. In the computation of a vortex sheet, a problem of uniqueness arises when dealing with multiply connected domains as happened in 2-D body. To obtain a unique solution in 2-D, the integral constraint of Kelvin's theorem can be imposed on the system of equations. The formulation of integral constraint is

$$\oint \underline{\Gamma}(s) \mathrm{d}s = -2A_B(\Omega(t + \Delta t) - \Omega(t)), \tag{24}$$

where A_B, Ω are the area and the rotation velocity of the wall panel, respectively. The system of Eqs. (23) and (24) will be discretized into wall panels and lead to a linear system

$$M\underline{\Gamma} = b. \tag{25}$$

where M is the coefficient matrix. The right hand side of this linear equation is represented by the slip velocity vector of the surface. The solution of the linear system (25) will be the input for the no-slip boundary condition, which is

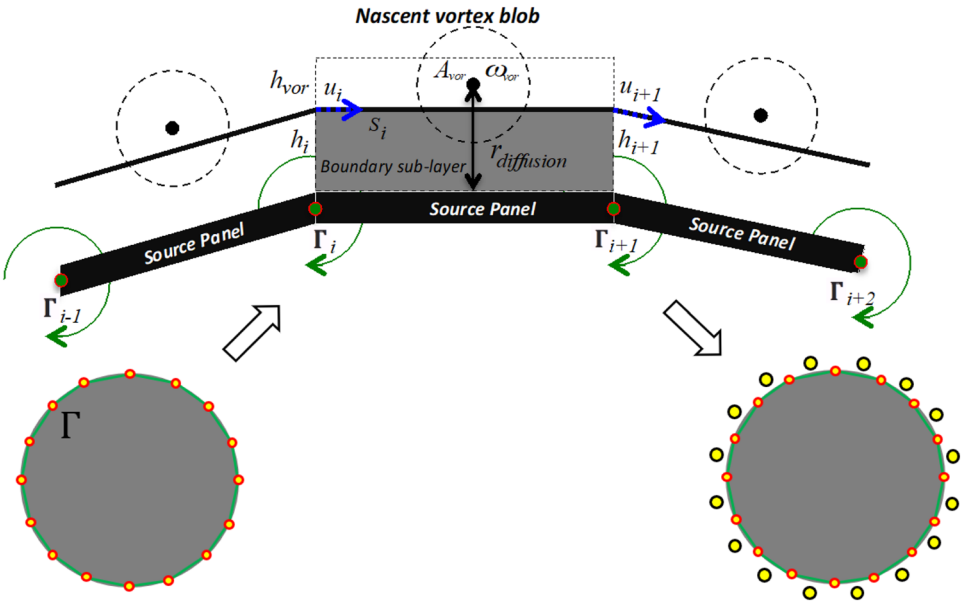

Fig. 5 Production of Nascent vortex elements

clearly depicted in Fig. 5. The figure shows the generation of Nascent vortex elements from the wall followed by the work of Kamemoto [25]. As expressed in the figure,S_i, h_i, u_i denote, respectively, length of an outer boundary element, vorticity layer thickness and tangential velocity at each node of the outer boundary.

The Nascent vortex element is convected and diffused by velocities: V_c and V_d, respectively, as follows:

$$V_c = \frac{1}{s_i}\left(\frac{h_i u_i}{2} - \frac{h_{i+1}u_{i+1}}{2}\right), \tag{26}$$

$$V_d = \frac{dr_{diffusion}}{dt} = \frac{1.136^2\nu}{r_{diffusion}} \tag{27}$$

where the height of boundary layer at certain panel i, h_i, is given by

$$h_i = r_{diffusion} = 1.136\sqrt{\nu\Delta t}. \tag{28}$$

The Nascent vortex element is then replaced by an equivalent vortex blob with an area A and vorticity ω_{vor} as given by the following relations,

$$h_{vor} = \left(V_c + V_d\right)\Delta t, \tag{29}$$

$$A_{vor} = h_{vor} \times s_i, \quad A = h_i \times s_i, \tag{30}$$

$$\omega_{vor} = \frac{\underline{\Gamma}}{A + A_{vor}}. \tag{31}$$

In Eq. (31), the circulation $\underline{\Gamma}$ is the strength of the vortex sheet, which satisfies no through boundary condition. Accordingly, the core size of the initial generated blob is calculated as

$$sig_{blob} = 2\sqrt{\frac{\Gamma}{\pi\omega_{vor}}}. \tag{32}$$

Once a Nascent vortex element is shed from the wall, a new vortex element is redistributed along the wall panel for the next time step. The new generation of the vortex elements satisfies the no-slip boundary and represents the boundary layer.

2.4 Aerodynamic forces and moments

The aerodynamic forces and moments computed from the present FLVM are the inputs for the calculation of the flutter derivatives. The classical technique to evaluate the lift and drag forces and moments acting on a body is to compute the time derivatives of the linear impulse [40, 41]. The linear impulse is based on the vorticity strengths of all particles in the flow field. This method is very robust and has an almost zero computational cost, as it is implemented as a sum running over all particles. Since the FLVM solver resolved the flow field with uniform resolution, the far wake could become well resolved; thereby the accuracy of linear impulse and forces is retained.

The lift and drag forces $\underline{F}\left(F_x, F_y\right)$ are computed based on the linear impulse $\underline{I}\left(I_x, I_y\right)$ as follows:

$$\underline{I} = \sum_{p=1}^{N} \underline{x}_p \, \underline{\Gamma}_p, \tag{33}$$

$$\underline{F} = \left(\frac{1}{2}\rho U_\infty^2 D\right) \frac{\underline{I}(t-\Delta t) - \underline{I}(t+\Delta t)}{\rho U_\infty^2 D \Delta t} = \frac{\underline{I}(t-\Delta t) - \underline{I}(t+\Delta t)}{2\Delta t}, \tag{34}$$

where ρ is the density. D is the characteristic length of the object. U_∞ is free stream velocity, Δt is the incremental time, and N is the number of particles. The pitching moment is calculated as follows:

$$\begin{aligned} \underline{M} &= \left(\frac{1}{2}\rho U_\infty^2 D^2\right)\left(\frac{\underline{A}(t+\Delta t) - \underline{A}(t-\Delta t)}{\rho U_\infty^2 D^2 \Delta t} - \frac{2\underline{B}}{\rho U_\infty D^2}\right) \\ &= \frac{\underline{A}(t+\Delta t) - \underline{A}(t-\Delta t)}{2\Delta t} - U_\infty \underline{B}, \end{aligned} \tag{35}$$

where $\underline{A} = 0.5 \sum_{p=1}^{N} \left|\underline{x}_p\right|^2 \underline{\Gamma}_p$ and $\underline{B} = (\cos(\alpha) I_x - \sin(\alpha) I_y)\hat{e}_z$. The vector $\hat{e}_z$ is the unit vector in z-direction (0, 0, 1) and α is the angle of attack (AoA). The computed aerodynamic forces in two-dimensional cases were expressed in non-dimensional form using the conventional normalization as follows

$$C_{\mathrm{D}} = \frac{F_y}{\frac{1}{2}\rho U_\infty^2 D}, \quad C_{\mathrm{L}} = \frac{F_x}{\frac{1}{2}\rho U_\infty^2 D}, \quad C_{\mathrm{M}} = \frac{M_z}{\frac{1}{2}\rho U_\infty^2 D^2} \tag{36}$$

$C_{\mathrm{D}}, C_{\mathrm{L}}, C_{\mathrm{M}}$ are drag, lift and moment coefficients in two-dimensional flow cases.

3 Numerical estimation of flutter derivatives and flutter speed

At the sufficiently high flow speed, flutter instability causes the structure undergoing a simple harmonic motion. Otherwise, the forces, developed due to a bluff or streamlined bodies undergoing time-dependent motion in a steady fluid flow, will also be harmonic. Hence, to predict the flutter instability, the aerodynamic coefficients of the flutter instability (flutter derivatives) are to be evaluated to model the harmonic fluid forces by prescribing the motion of a body to be purely translational or purely rotational. Otherwise, the critical flutter speed of the obstacles, which is an essential parameter for the engineering designs, is calculated based on these computed flutter derivatives.

3.1 Determination of flutter derivatives

Flutter derivatives are analytically obtained using Theodorsen's function [42]. Scanlan and Tomko [1] proposed a formulation of motion-induced aerodynamic forces and moment suitable for two-dimensional cross sections from wind tunnel tests involving six flutter derivatives. Larsen and Walther [20] proposed a logical extension with eight flutter derivatives. Motivated by the works of Morgenthal [21] and Walther and Larsen [43], this work utilizes the Larsen's extension formulation for predicting flutter derivatives of various bridge cross sections using a numerical experiment. Accordingly, the unsteady aerodynamic force and moment acting on a single body can be linearly expressed as follows:

$$F_x = \rho U_\infty^2 D\left[KH_1^* \frac{\dot{h}}{U_\infty} + KH_2^* \frac{D\dot{\alpha}}{U_\infty} + K^2 H_3^* \alpha + K^2 H_4^* \frac{h}{D}\right], \tag{37}$$

$$M_z = \rho U_\infty^2 D^2\left[KA_1^* \frac{\dot{h}}{U_\infty} + KA_2^* \frac{D\dot{\alpha}}{U_\infty} + K^2 A_3^* \alpha + K^2 A_4^* \frac{h}{D}\right], \tag{38}$$

where $K = 2\pi f D/U_\infty$ is reduced frequency and f is the frequency of harmonic translational or rotational motions. $h, \dot{h}$ are translational motion and its time derivative and $\alpha, \dot{\alpha}$ are rotational angle around a base and its time derivative. $H_j^*, A_j^*, j = 1, \ldots, 4$ are flutter derivatives which are basically modeled as a function of K. The flutter derivatives are dependent on reduced velocity $\left(U_\theta = \frac{U_\infty}{fD} = \frac{2\pi}{K}\right)$ for a single body. By prescribing the translational motion $\left(h(t) = A_h \sin(2\pi f t)\right)$ or the rotational motion $\left(\alpha(t) = A_\alpha \sin(2\pi f t)\right)$ force F_x and moment M_z on the body are directly computed from the FLVM solver using Eqs. (34) and (35), respectively. Equations (37) and (38) are reduced to

$$\rho U_\infty^2 D\left[KH_1^* \frac{\dot{h}}{U_\infty} + K^2 H_4^* \frac{h}{D}\right] = F_x \tag{39}$$

$$\rho U_\infty^2 D^2\left[KA_1^* \frac{\dot{h}}{U_\infty} + K^2 A_4^* \frac{h}{D}\right] = M_z \tag{40}$$

for purely translational motion, and

$$\rho U_\infty^2 D\left[KH_2^* \frac{D\dot{\alpha}}{U_\infty} + K^2 H_3^* \alpha\right] = F_x \tag{41}$$

$$\rho U_\infty^2 D^2\left[KA_2^* \frac{D\dot{\alpha}}{U_\infty} + K^2 A_3^* \alpha\right] = M_z, \tag{42}$$

for purely rotational motion. The flutter derivatives $(H_1^*, H_4^*, A_1^*, A_4^*)$ can be, therefore, solved by a linear system as

$$\left(\frac{K\dot{h}_1}{U_\infty}\frac{K^2 h_1}{D} \cdots \cdots \frac{K\dot{h}_n}{U_\infty}\frac{K^2 h_n}{D}\right)\left(H_1^* H_4^*\right) = \left(\frac{F_x^1}{\rho U_\infty^2 D} \cdots \frac{F_x^n}{\rho U_\infty^2 D}\right) \tag{43}$$

and

$$\left(\frac{K\dot{h}_1}{U_\infty}\frac{K^2h_1}{D}\ \cdots\ \cdots\ \frac{K\dot{h}_n}{U_\infty}\frac{K^2h_n}{D}\right)\left(A_1^*A_4^*\right)=\left(\frac{M_z^1}{\rho U_\infty^2D^2}\cdots\frac{M_z^n}{\rho U_\infty^2D^2}\right) \tag{44}$$

for purely translational motion. The number, n, indicates the number of iteration samples at every time step of the simulation that records instantaneously the translational displacement h_j, its time derivative $\dot{h}_j$, lift force F_x^j, and moment $M_z^j, j=1,\ldots,n$. Similarly, the flutter derivatives $(H_2^*, H_3^*, A_2^*, A_3^*)$ can be, therefore, solved by a linear system as

$$\left(\frac{K\dot{\alpha}_1}{U_\infty}K^2\alpha_1\ \cdots\ \cdots\ \frac{K\dot{\alpha}_n}{U_\infty}K^2\alpha_n\right)\left(H_2^*H_3^*\right)=\left(\frac{F_x^1}{\rho U_\infty^2D}\cdots\frac{F_x^n}{\rho U_\infty^2D}\right) \tag{45}$$

and

$$\left(\frac{K\dot{\alpha}_1}{U_\infty}K^2\alpha_1\ \cdots\ \cdots\ \frac{K\dot{\alpha}_n}{U_\infty}K^2\alpha_n\right)\left(A_2^*A_3^*\right)=\left(\frac{M_z^1}{\rho U_\infty^2D^2}\cdots\frac{M_z^n}{\rho U_\infty^2D^2}\right) \tag{46}$$

for purely rotational motion. The linear matrix systems (43), (44), (45), and (46) are solved using least squares technique according to the work listed in the reference [43].

3.2 Determination of flutter speed

According to linear expression of force and moment (34) and (35), the fully physical system of the heaving and pitching body can be expressed as

$$\ddot{h}+2\zeta_hK_h\dot{h}+K_h^2h=\frac{\rho U_\infty^2D}{n_h}\left[KH_1^*\frac{\dot{h}}{U_\infty}+KH_2^*\frac{D\dot{\alpha}}{U_\infty}+K^2H_3^*\alpha+K^2H_4^*\frac{h}{D}\right], \tag{47}$$

$$\ddot{\alpha}+2\zeta_\alpha K_\alpha\dot{\alpha}+K_\alpha^2\alpha=\frac{\rho U_\infty^2D^2}{n_\alpha}\left[KA_1^*\frac{\dot{h}}{U_\infty}+KA_2^*\frac{D\dot{\alpha}}{U_\infty}+K^2A_3^*\alpha+K^2A_4^*\frac{h}{D}\right], \tag{48}$$

where ζ_h, ζ_α are the structural damping ratios. $K_h=\frac{2\pi Df_h}{U_\infty}$, $K_\alpha=\frac{2\pi Df_\alpha}{U_\infty}$ in which f_h, f_α are the circular natural frequencies of the body for translational and rotational oscillation, respectively. $n_h=\frac{m}{\rho D^2}$ is mass ratio and $n_\alpha=\frac{I}{\rho D^4}$ is the ratio of inertia moment. To predict the flutter instability at the certain frequency K, the translational and rotational oscillations are assumed to be harmonic with the same frequency K of the vortex shedding of the flow as

$$h(t)=A_he^{iKt}, \tag{49}$$

$$\alpha(t)=A_\alpha e^{iKt}. \tag{50}$$

A_h, A_α are translational and rotational magnitudes, respectively. Then, substituting Eqs. (49) and (50) into Eqs. (47) and (48) and representing in the matrix format, two Eqs. (47) and (48) are reduced to

$$\begin{bmatrix}A & B & C & D\end{bmatrix}\begin{bmatrix}A_h & A_\alpha\end{bmatrix}=\begin{bmatrix}0 & 0\end{bmatrix}, \tag{51}$$

where

$$A=-K^2+2\zeta_hK_hKi+K_h^2-\frac{\rho U_\infty D}{n_h}K^2H_1^*i-\frac{\rho U_\infty^2}{n_h}K^2H_4^*, \tag{52}$$

$$B=\frac{\rho U_\infty D^2}{n_h}K^2H_2^*i-\frac{\rho U_\infty^2D}{n_h}K^2H_3^*, \tag{53}$$

$$C=-\frac{\rho U_\infty D^2}{n_\alpha}K^2A_1^*i-\frac{\rho U_\infty^2D}{n_\alpha}K^2A_4^* \tag{54}$$

$$D=-K^2+2\zeta_\alpha K_\alpha Ki+K_\alpha^2-\frac{\rho U_\infty D^3}{n_\alpha}K^2A_2^*i-\frac{\rho U_\infty D^2}{n_\alpha}K^2A_3^*. \tag{55}$$

To solve the linear system with non-trivial solution, the constraint, including the zero determinant of the matrix solution system, is considered as

$$AD-CB=0. \tag{56}$$

The solution of Eq. (56) is then evaluated to determine K, which is considered as a complex number $K=K_\mathrm{R}+iK_\mathrm{I}$.

The real part K_R represents the frequency of the oscillation and the imaginary part K_I indicates whether the oscillation of the body is decaying or growing. The positive K_I suggests the decaying oscillation and the negative represents the growing oscillation.

4 Computational setup

To validate the performance of the FLVM solver, the simulations of flow over an impulsively started circular cylinder are performed at Reynolds number $\left(Re=\frac{U_\infty D}{\nu}=550\right)$,

where ν is kinematic viscosity. In this case, M is set to be 5 for the splitting scheme, ε and α are set to be equal to 1 and 0.85, respectively and $\Gamma_{\text{ref}} = U_\infty D$ for a merging scheme. The initial parameters for the simulation are listed in Table 1.

In this solver, the Reynolds number is the one of the primary input parameters for simulation. Small time step Δt reduces the number of merging events in the same time period of simulation. Accordingly, the error in merging events is spatially decreased within the simulation time. The number of panels determines the initial vorticity surrounding the wall through the introduction of Nascent vortex elements. This vorticity layer apparently represents the no-though boundary condition, which is the input for the no-slip boundary condition to resolve the boundary layer. The accuracy and the stability of the FLVM solver obviously depend on these initial conditions.

Table 1 Input parameters

Re	Δt(time step)	Panels
550	0.01(s)	500

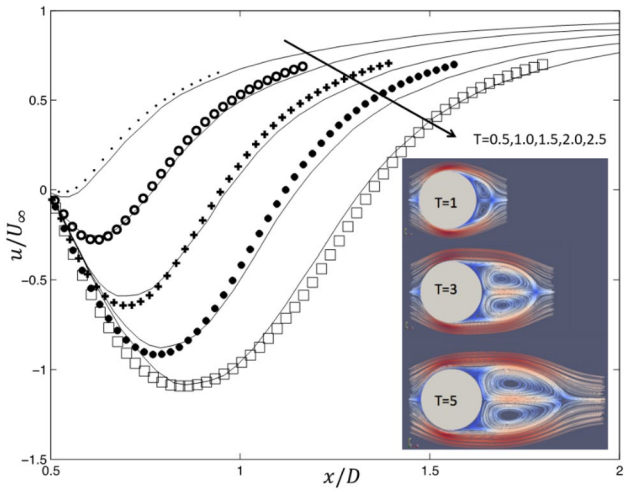

Fig. 6 Velocity distributions along the horizontal centerline and contours of velocity streamline colored by magnitude of velocity vector at different times. *Symbols* denote present results and *continuous lines* denote experimental data [37]

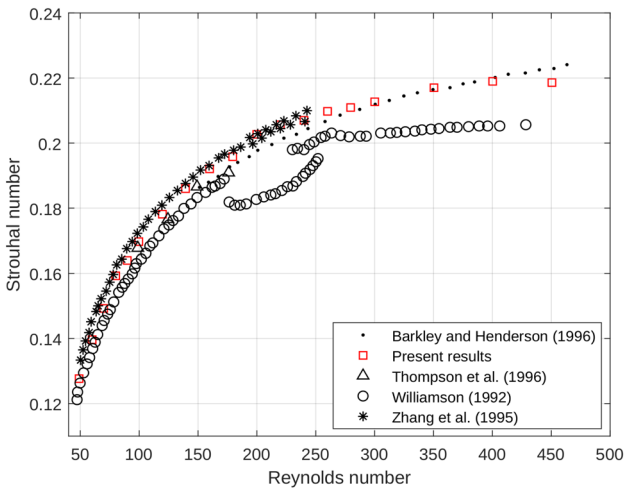

Fig. 7 Strouhal number versus Reynolds number variation of flow around a circular cylinder

Table 2 Convergence study of spatial resolutions

Resolutions	Coarse	Medium	Fine
Particle core size (σ_p)	$\sqrt{15\frac{U_\infty D}{Re}\Delta t}$	$\sqrt{10\frac{U_\infty D}{Re}\Delta t}$	$\sqrt{6\frac{U_\infty D}{Re}\Delta t}$
$\frac{\max\lvert C_D - C_{D,FINE}\rvert}{\max\lvert C_{D,FINE}\rvert}$	7.5%	5.5%	

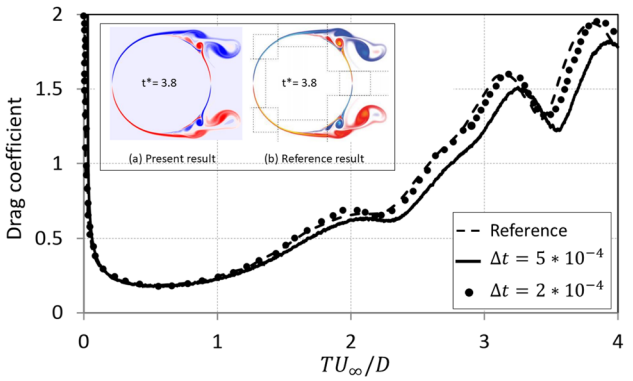

Fig. 8 Vorticity contours and drag force coefficient of the impulsively started flow around a stationary circular cylinder at $Re = 9500$. *Dashed line* is the result of Rasmussen et al. [50]. *Dotted line* is the present result at $\Delta t = 2 * 10^{-4}$. *Continuous line* is the present result at $\Delta t = 5 * 10^{-4}$

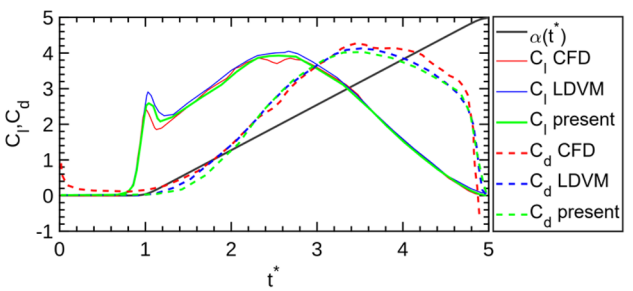

Fig. 9 The case study I (flow past a pitching flat plate with the maximal pitching angles 90°, $Re = 1000$). Lift and drag coefficients from CFD by Kinsey and Dumas [52], LDVM by Ramesh et al. [53], and FLVM follows the scale of the left-hand axis. The right-hand axis shows the scale from 0° to 90° for pitching angles $\alpha(t^*)$

Figure 6 shows velocity distributions along the horizontal centerline and contours of velocity streamline colored by magnitude of velocity vector at different times $\left(t^* = \frac{TU_\infty}{D} = 1, 3, 5\right)$. Symbols denote present results and continuous lines denote experimental data [37]. The computed centerline velocity in the recirculating flow region is in good agreement with those obtained by the experiment data. The contours of velocity streamline illustrate quantitatively the development of a symmetrical wake behind the cylinder from the initial stage until the later stages of the simulation ($t^* = 5$).

As depicted by the figure, a pair of vortex bubbles steadily developed into larger bubbles during simulation time. In the contour of velocity streamline, the separation point is found to be located around 60°, which agrees well with the numerical result of Kim [44] and the experimental result of Taneda [45].

Figure 7 illustrates the change of Strouhal number with the *Re* variation in the case of flows past a circular cylinder. The present results agree well with those given by Zhang et al. [46] and Barkley and Henderson [47]; however, they show slight differences with those provided by Williamson [48] and Thompson et al. [49].

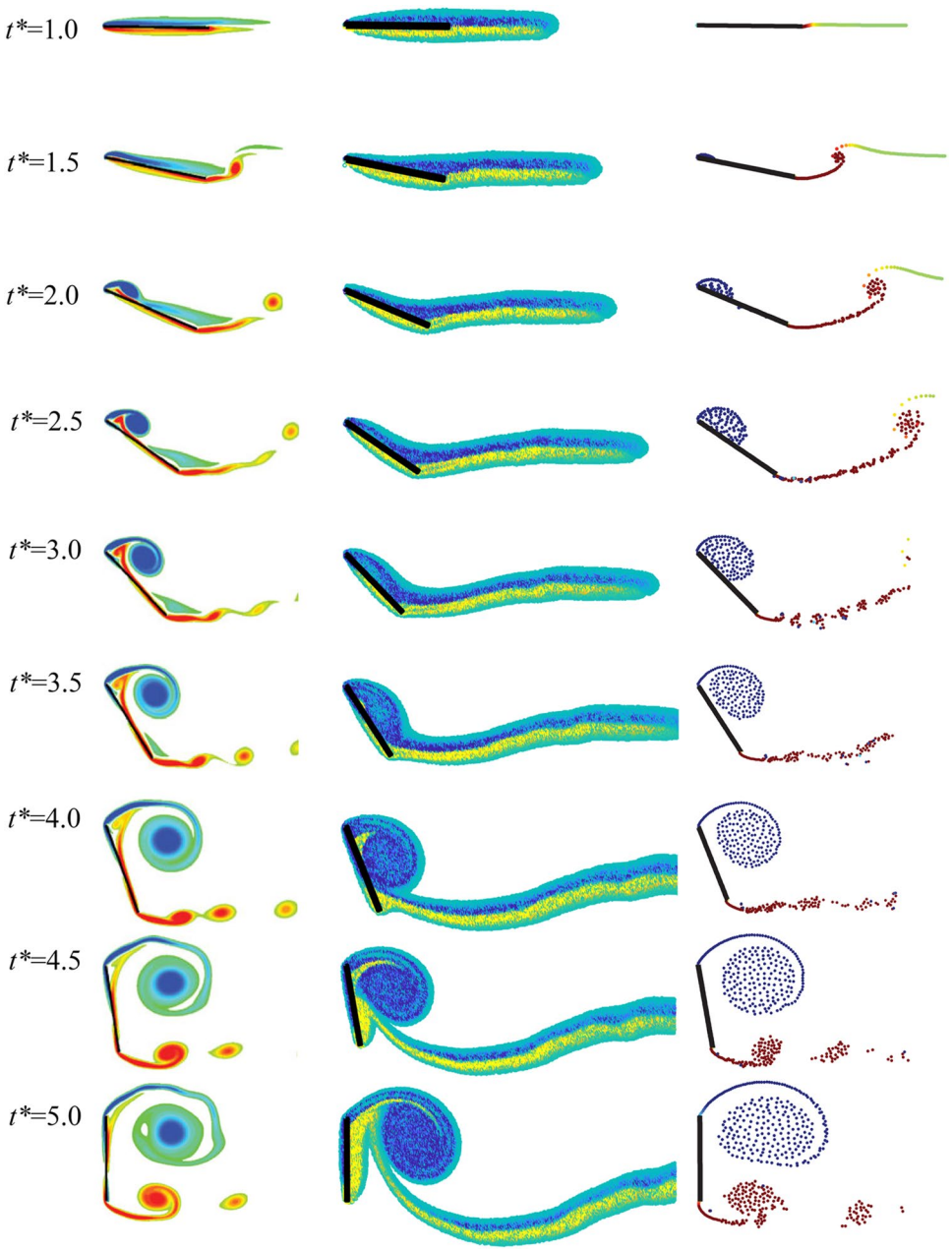

Fig. 10 The case study I (flow past a pitching flat plate with the maximal pitching angles 90°, $Re = 1000$). Flow features from CFD by Kinsey and Dumas [52] (left-hand column), LDVM by Ramesh et al. [53] (right-hand column), and FLVM (middle column)

For the convergence study of spatial resolution shown in Table 2, the medium size particle core size provides sufficient resolution to achieve spatial convergence, while the coarse core size produces the insufficient spatial resolution. For all cases that follow, the resolution used in this study is based on the medium resolution to reduce its computational cost and to resolve sufficiently the flowfield.

For the temporal convergence study, Fig. 8 shows vorticity contours and drag force coefficient of the impulsively started flow around a stationary circular cylinder at $Re = 9500$. Dashed line is the reference result by Rasmussen et al. [50]. Dotted line is the present result at $\Delta t = 2 * 10^{-4}$. Continuous line is the present result at $\Delta t = 5 * 10^{-4}$. As shown by the vorticity contours, the present result expresses the good agreement with the reference result in capturing the primary and secondary vortex structures generated from the cylinder boundary at $t^* = 3.8$. The qualitative results of drag coefficient obtained with different incremental times also show a small deviation with the reference. In particular, the present results at smaller Δt approach the reference results better than those at larger Δt. Hence, these evidences prove that the current FLVM solver captures well the characteristics of the flow around a bluff body.

5 Two-dimensional flapping wing models at high frequencies

In this section, flat plate with rectangular platform with the characteristic length $D = 1$ undergoing pitching maneuvers and NACA 0030 airfoil with the characteristic chord $C = 1$ under heaving and pitching maneuvers in a characteristic velocity $U_\infty = 1$ are considered to verify the validity of the FLVM solver for the simulation of flows past oscillating obstacles at high frequencies.

The pitching flat plate is investigated with two pitching reduced frequencies including $K = 0.785$(case I) and $K = 0.3925$ (case II). The heaving and pitching airfoil is carried out with two Reynolds numbers including $Re = 240$ (case III) and 480 (case IV). The Reynolds number is chosen to take into account issues of high frequency oscillating motions and to highlight the high resolution of large-scale wake structures generated by the unsteady motions of the obstacles. In the present simulations, the $Re = 1000$ is considered for the cases of pitching flat plates. The unsteady pitching maneuvers are defined by the function proposed by Eldredge [51]. The function defines a smoothed linear rate of change of AoA, which allows for a continuous motion and avoids discontinuity in angular acceleration.

$$\alpha(t^*) = \frac{\alpha_0 D}{2aU_\infty\left(t_2^* - t_1^*\right)}\log\left(\frac{\cosh\left(\frac{aU_\infty\left(t^*-t_1^*\right)}{D}\right)}{\cosh\left(\frac{aU_\infty\left(t^*-t_2^*\right)}{D}\right)}\right) - \frac{aU_\infty\left(t_1^* - t_2^*\right)}{D}. \tag{57}$$

In the Eq. (57), a controls the smoothing of pitching acceleration. α_0 is the maximum rotational angle in radians. The dimensionless quantities, t_1^* and $t_2^* = t_1^* + \alpha_0\frac{D}{(2U_\infty K)}$ are start-up and end-up times of the unsmoothed motion, respectively. In case I, α_0, t_1^*, and a are set to be $\frac{\pi}{2}$, 1, and 5.2 while in the case II those parameters are fixed as $\frac{\pi}{4}$, 1, and 11 .

In the cases III and IV, the heaving and pitching motions of the NACA 0030 are defined as sinusoidal function for both translational ($h(t^*) = h_0\sin(2\pi f t^*)$) and rotational ($\alpha(t^*) = \alpha_0\cos(2\pi f t^* + \phi)$) modes. Two simulations are performed with the same frequency $f = \frac{KU_\infty}{2\pi C} = \frac{1}{2\pi}$, $\alpha_0 = 20°$, and $\phi = 75°$. The airfoil is heaved and pitched about one-third chord length away from the leading edge.

Figure 9 depicts the present qualitative results of case study I. Lift and drag coefficients from CFD by Kinsey and Dumas [52], LDVM by Ramesh et al. [53], and FLVM follows the scale of the left-hand axis. The right-hand axis shows the scale from 0° to 90° for pitching angles $\alpha(t^*)$. As shown by the figure, the lift and drag coefficients of the present results express slight deviation with the CFD results and LDVM results. In addition, the maximal peaks of C_d

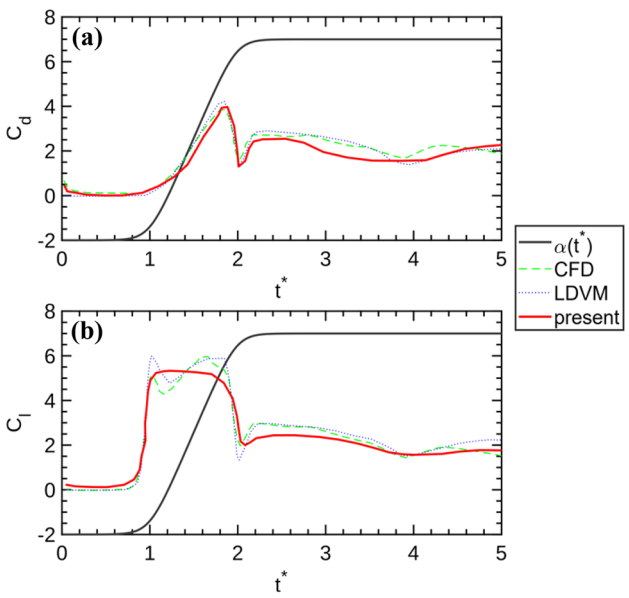

Fig. 11 The case study II (flow past a pitching flat plate with the maximal pitching angles 45°, $Re = 1000$). Lift and drag coefficients from CFD by Kinsey and Dumas [52], LDVM by Ramesh et al. [53], and FLVM follows the scale of the left-hand axis. The right-hand axis shows the scale from 0° to 50° for pitching angles $\alpha(t^*)$

and C_L of the present results during the pitching motions are identical with references.

Figure 10 shows the quantitative comparison of the case study I with references listed in literature. Flow features related to vorticity contours from CFD by Kinsey and Dumas [52] (left-hand column), LDVM by Ramesh et al. [53] (right-hand column), and present FLVM (middle column) are arranged in the figure. The formation and detachment of the leading edge vortex (LEV) are in a good agreement with the results obtained by references. Specifically, the LEV is captured with the identical position and size with those observed by reference solvers during the pitching motion. The presence of LEV correlates with the cause of enhanced lift coefficient obtained in the previous figure. Figure 11 depicts the case study II. Lift and drag coefficients from CFD by Kinsey and Dumas [52], LDVM by Ramesh et al. [53], and FLVM follows the scale of the left-hand axis. The right-hand axis shows the scale from 0^0 to 50^0 for pitching angles $\alpha(t^*)$.

The present C_d and C_L are identical with those computed by references. The peak of C_L during the pitching maneuver shows slight difference with reference results while the peak of C_D approaches well with the reference results. Figure 12 describes the vorticity contours for the case study II. Flow features from CFD by Kinsey and Dumas [52] (left-hand column), LDVM by Ramesh et al. [53] (right-hand column), and FLVM (middle column) are presented. The formation and the detachment of the leading edge vortex and trailing

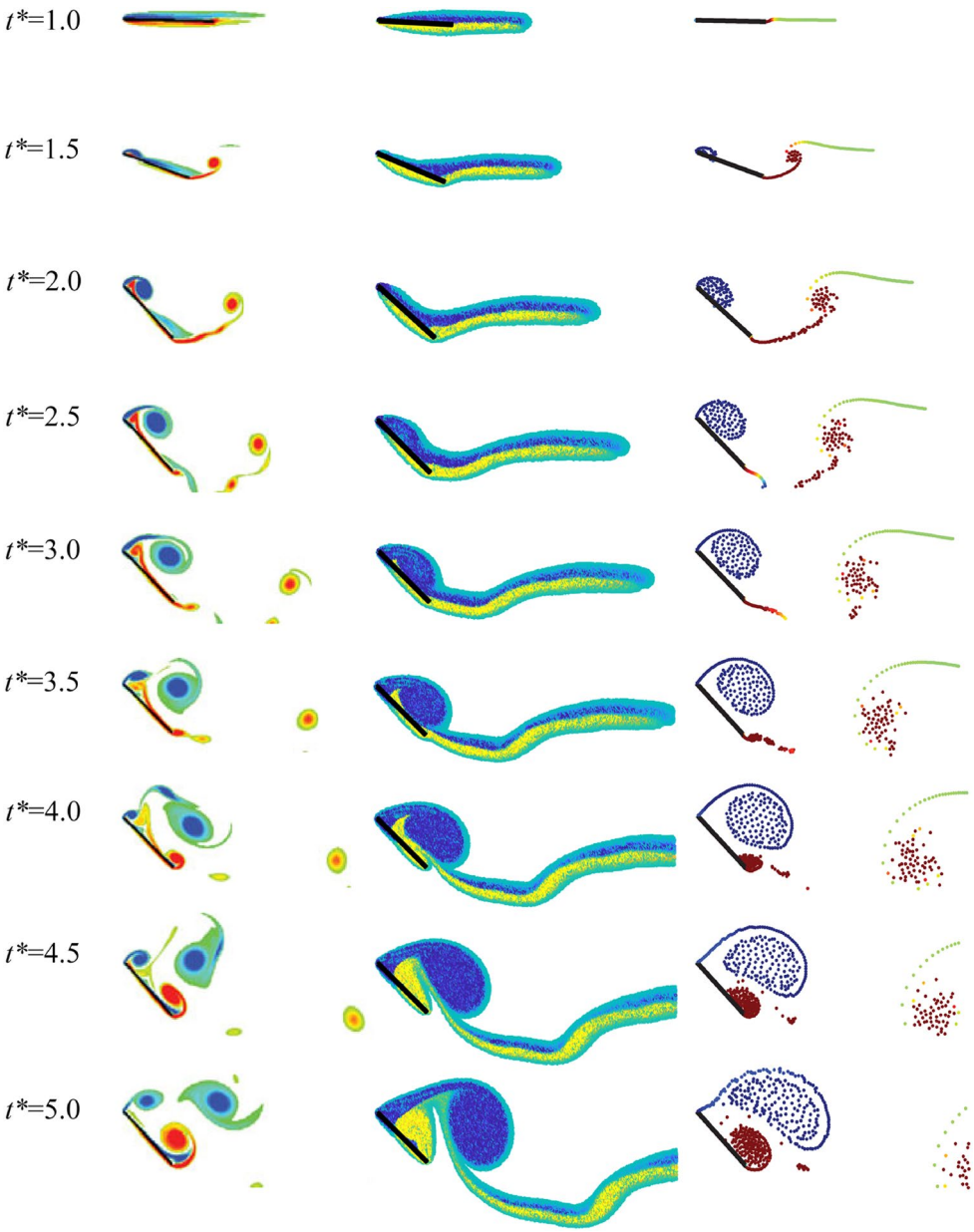

Fig. 12 The case study II (flow past a pitching flat plate with the maximal pitching angles 45°, $Re = 1000$). Flow features from CFD by Kinsey and Dumas [52] (left-hand column), LDVM by Ramesh et al. [53] (right-hand column), and FLVM (middle column)

edge vortex (TEV) of the present results are observed to be identical with those obtained from references. The sizes and positions of the LEV and TEV of the present results are identical with LDVM results. Figures 13 and 14 show the case studies III and IV, respectively. The flow features of vorticity contours are shown at phases $(0, \frac{\pi}{2}, \pi, \frac{3\pi}{2})$ from left- to right-hand figures, respectively.

The upper side row is the reference results from Yu et al. [54]. The lower side row is the present FLVM results. As described by these figures, the vortex bubbles shedding behind the NACA 0030 airfoil of the present results for different phases of oscillation are similar to those captured by the reference. The differences of thrust coefficients between current and reference results can be apparently seen in Fig. 15. The red-colored lines are the results from Yu et al. [54]. The blue-colored lines are the results from the present FLVM solver. It is fair to conclude that the FLVM solver can capture well large-scale vortex structures developed behind the bluff body under heaving and pitching motions with high-frequency oscillations.

6 Determination of flutter derivatives and flutter speed

The numerical experiments below follow the same methodology described in the previous section. The flat plate is forced to prescribed oscillations and the computations are carried to go beyond several periods of oscillation. The fluid forces recorded on the last period to extract the corresponding flutter derivatives. Then, the flutter speed of the oscillating flat plate is numerically determined.

6.1 Forced-oscillating flat plate

To numerically calculate flutter derivatives of a flat plate, forced-translation and forced-rotation flat plate are simulated using initial conditions listed in Table 3.

The forced motions of the plate are defined as sinusoidal function for both translational $(h(t^*) = A_h\cos(2\pi f t^*))$ and rotational $(\alpha(t^*) = A_\alpha\cos(2\pi f t^*))$ modes. The simulation is performed in a limited range of frequency of the vertical and rotational motions $f = 0.1,\ 0.143,\ 0.25,\ 0.5,\ 1$. Using 208 boundary elements, the flat plate is oscillated in heave and pitch about the half-chord $(x_\alpha = 0)$ with an amplitude $A_h = 0.05$, and $A_\alpha = 5^o$, respectively. The configuration of the simulation is depicted in Fig. 16.

Figure 17 depicts time history of aerodynamic lift and moment coefficients for flow past a flat plate in pitching motion at $Re = U_\infty D/\nu = 500,\ 1000,\ 3000$, where D is the characteristic length of the flat plate. The figure suggests that the moment coefficients do not deviate from each other at three different Reynolds numbers. Otherwise, the lift coefficient shows a difference at the peak. The higher Reynolds numbers demonstrate a little higher peaks of lift coefficient. It is fair to say that the lift and moment coefficients do not show a significant difference in the range of Reynolds numbers from 500 to 3000. Hence, the Reynolds number $Re = 1000$ is selected in the following simulations due to its independence to the evaluation of aerodynamic coefficients.

Figure 18 shows the time history of corresponding aerodynamic lift and moment coefficients for flow past a flat plate in pitching motion at $Re = 1000$. $U_\theta = 1$. Dashed lines are results from FLVM solver and the solid lines are modeled lift (red) and moment (blue) coefficients from

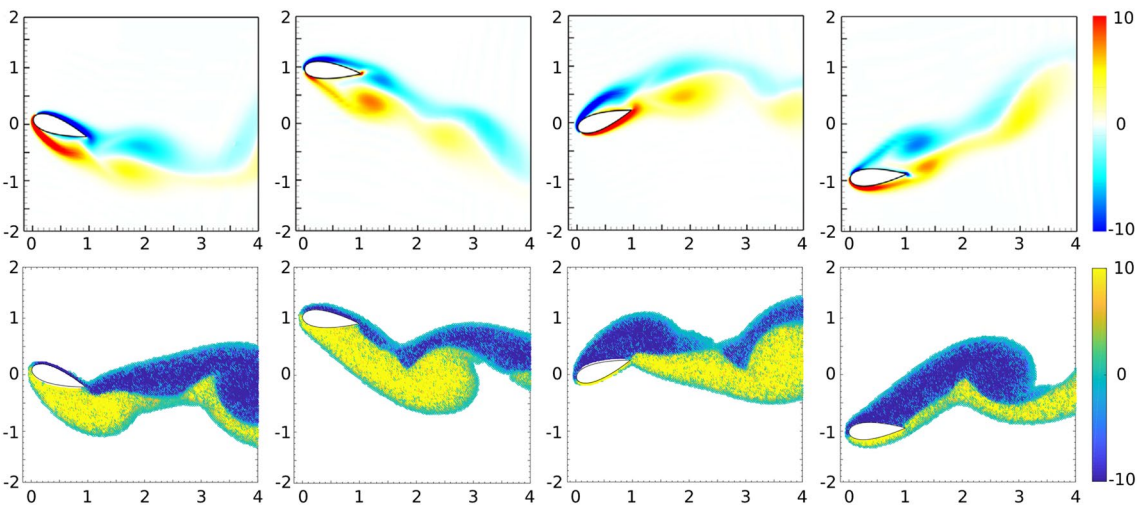

Fig. 13 Case study III (vorticity contours for the NACA0030 airfoil with the heaving and pitching motion at $Re = 240$). From left- to right-hand vorticity contours at phases 0; $\frac{\pi}{2}$; π; $\frac{3\pi}{2}$, respectively. The upper side row is the results from Yu et al. [54]. The lower side row is the FLVM results

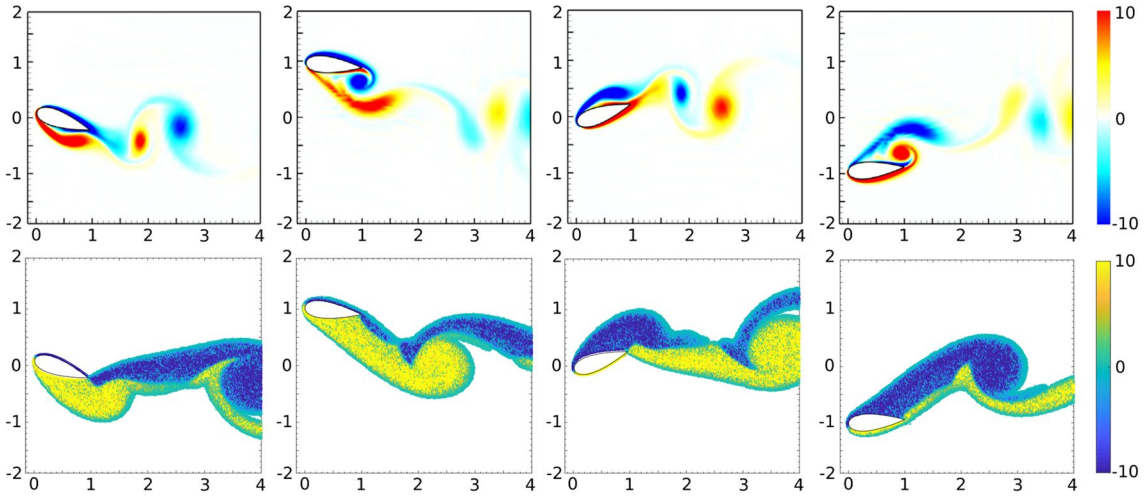

Fig. 14 Case study IV (vorticity contours for the NACA0030 airfoil with the heaving and pitching motion at $Re = 480$). From left- to right- hand vorticity contours at phases 0; $\frac{\pi}{2}$; π; $\frac{3\pi}{2}$, respectively. The upper side row is the results from Yu et al. [54]. The lower side row is the results from FLVM

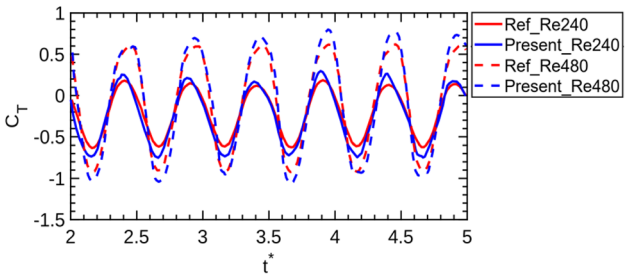

Fig. 15 Time histories of the thrust coefficients for a series of heaving and pitching NACA0030 airfoil at $Re = 240$ and 480. The *red-colored lines* are the results from Yu et al. [54]. The *blue-colored lines* are the results from FLVM

Eqs. (37) and (38). Figure 19 depicts the calculated flutter derivatives ($H_1^* - H_4^*$ and $A_1^* - A_4^*$) versus reduced velocity ($U_\theta = 0.1, 0.143, 0.25, 0.5, 1$) for flow past a flat plate at $Re = 1000$. The results of $A_1^*, A_2^*, A_4^*, H_1^*, H_2^*, H_4^*$ tend to deviate from the analytical solutions for higher reduced velocities due to the viscous effect resolved in the FLVM solver. In particular, the formation and detachment process of vortex structures is retarted due to viscosity and forced-motions with high amplitude producing some deviation to the computation of the flutter derivatives. These damping coefficients are generally difficult to be predicted correctly while the stiffness coefficients (especially A_3^*, H_3^*) are, in general, in a good agreement with the Theodorsen's solutions [42]. In addition, it is important to remember that the analytical solution is obtained by imposing the linearity assumption.

By solving Eq. (56) with respect to K using the computed flutter derivatives, the evaluation of flutter speed is shown in the Fig. 20, which depicts the plot of imaginary part (K_i) of reduced frequency versus reduced velocity (U_θ). The continuous line is interpolated using the least square method based on the dashed line data. From the plot, it is estimated that the value of K_i equals to zero when U_θ is approximately equal to 6(m/s) which is less than 4% of error compared to theoretical prediction of 6.21(m/s), which is listed in [42]. The difference is due to the deviations of flutter derivatives ($A_1^*, A_2^*, A_4^*, H_1^*, H_2^*, H_4^*$) with the inviscid theory, shown by the Fig. 19.

7 Conclusions

In the present study, the purely fast Lagrangian vortex method (FLVM) is developed to simulate the external incompressible flows past heaving and pitching bodies with high frequency oscillation. Due to the meshfree characteristics of the method, the vortical flows are freely tracked by local velocities and vorticities of particles introduced within the fluid domain. The Nascent vortex element is introduced to the flow field to retain the purely Lagrangian characteristics of the solver. The viscous effect is modeled using a core spreading method coupled with the splitting and merging spatial adaptation scheme to resolve

Table 3 Input parameters of forced-oscillating flat plate

Re	Δt	Panels	f_h	f_α	n_h	n_α	α(AoA)	x_α
1000	0.01 (s)	206	0.174	0.4	14.5	1.83	0	0

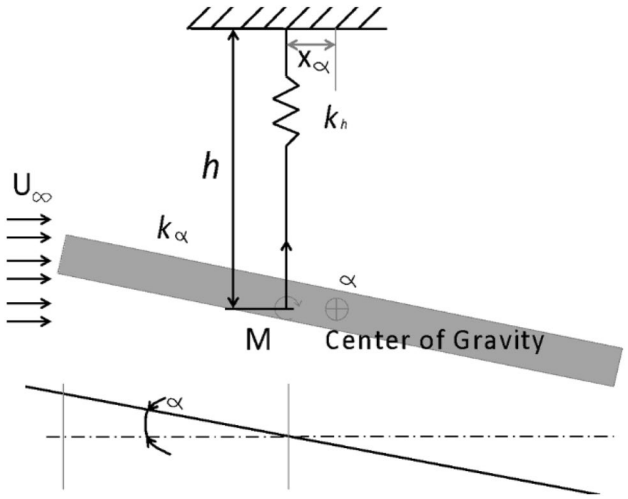

Fig. 16 Configuration of the forced-oscillating flat plate simulation

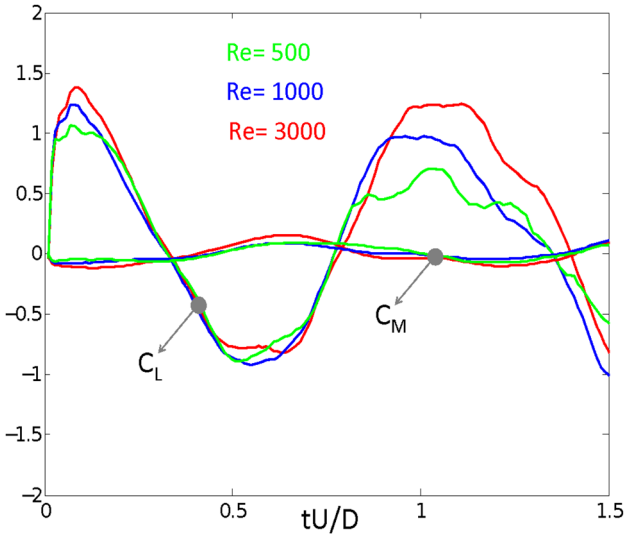

Fig. 17 Time history of aerodynamic lift and moment coefficients for flow past a flat plate in pitching motion at $Re = 500,\ 1000,\ 3000$

the boundary layer induced by solid walls. The particle's velocity is calculated using Biot–Savart formulation, which is accelerated by a fast multipole method (FMM).

The validity of the present algorithm is verified by temporal and spatial convergence studies for the case of flows past an impulsively started cylinder at the Reynolds numbers ranging from 50 to 9500. The drag coefficients and contours of velocity streamline are found to be in good agreement with those reported in literature.

The numerical algorithm of FLVM is then applied for the simulation of flows around the pitching flat plate with two pitching reduced frequencies $K = 0.785$ and 0.3925. For the

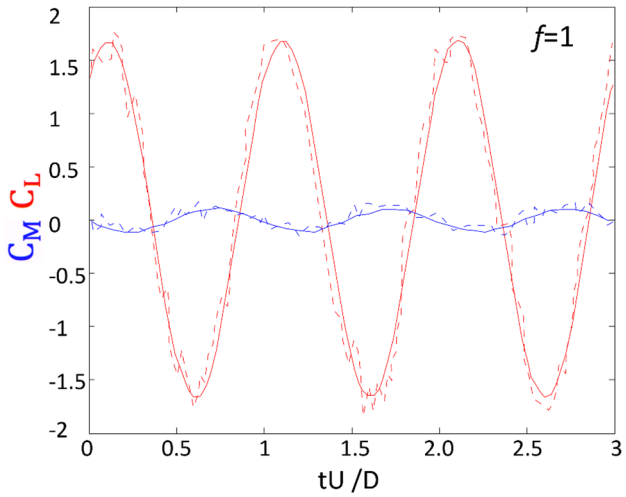

Fig. 18 Time history of aerodynamic lift and moment coefficients for flow past a flat plate in pitching motion at $Re = 1000$. $U_\theta = 1$. *Dashed lines* are results from FLVM solver and the solid lines are modeled lift (*red*) and moment (*blue*) coefficients

case of $K = 0.785$, the present time history results of drag and lift coefficients are in a good agreement with the reference results. Due to the formation of leading edge vortex (LEV), the maximal peaks of C_d and C_L of the present results during the pitching motions are also identical with those reported in references. For the case of $K = 0.3925$, the peak of C_L during the pitching maneuver shows slight difference with reference results while the peak of C_D approaches well with the reference results. The formation and the detachment of the leading edge vortex (LEV) and trailing edge vortex (TEV) of the present results are observed to be identical with those obtained from references.

The solver is then extended to the simulation of flows past a heaving and pitching airfoil with high frequency of oscillation. The vortex bubbles shedding behind the NACA 0030 airfoil of the present results for different phases of oscillation are similar to those captured by the reference. It is fair to conclude that the FLVM solver can capture well large-scale vortex structures developed behind the bluff body under heaving and pitching motions with high frequency oscillations.

The simulation scheme is then applied to compute the flutter derivatives and flutter speed of an oscillating flat plate at $Re = 1000$. The results of $A_1^*, A_2^*, A_4^*, H_1^*, H_2^*, H_4^*$ tend to deviate from the analytical solutions for higher reduced velocities due to the viscous effect resolved in the FLVM solver; while the stiffness coefficients (especially A_3^*, H_3^*) are, in general, in a good agreement with the inviscid theory. In particular, the formation and detachment of vortex structures is retarted in viscous fluids producing some deviation to the computation of the flutter derivatives.

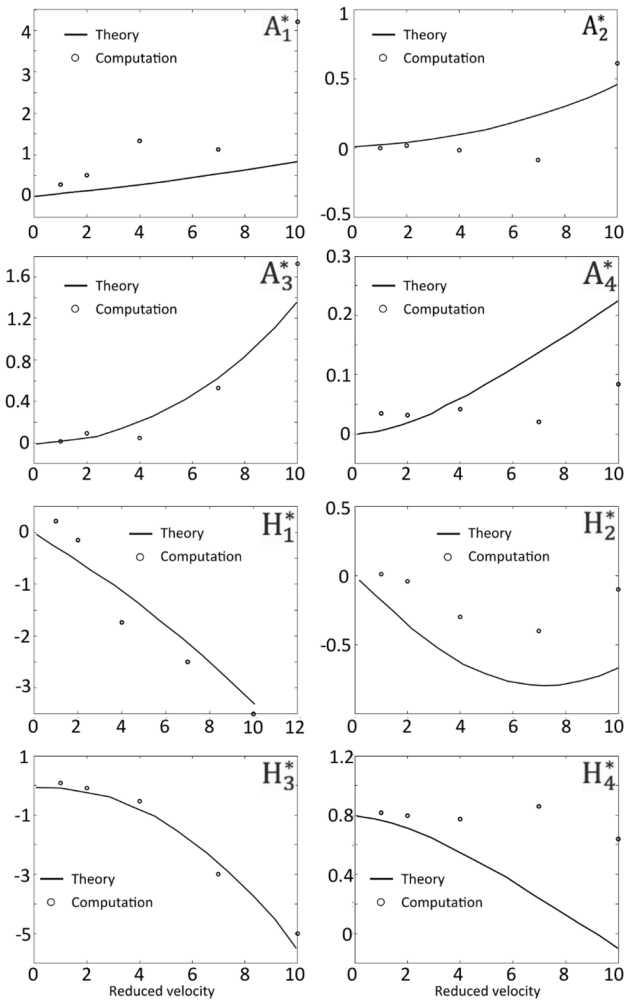

Fig. 19 Flutter derivatives versus reduced velocity ($U_\theta = 0.1, 0.143, 0.25, 0.5, 1$) for flow past a flat plate at $Re = 1000$. *Symbols* denoting computational results and *solid line* for analytical solution [42]

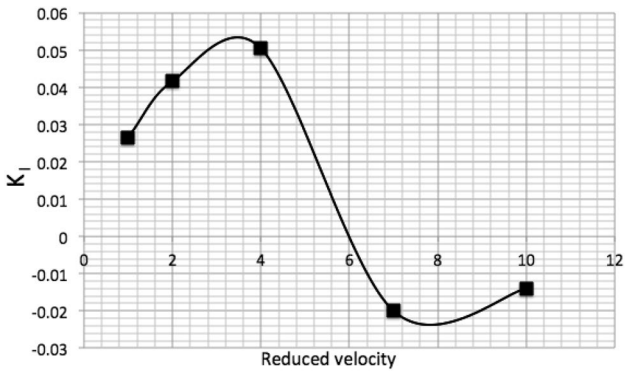

Fig. 20 Plot of imaginary part of flutter reduced frequency versus reduced velocity for flow past a flat plate at $Re = 1000$

References

1. Scanlan, R.H., Tomo, J.: Airfoil and bridge deck flutter derivatives. J. Eng. Mech. Div. **97**(6), 1717–1737 (1971)
2. Larsen, A.: Prediction of aeroelastic stability of suspension bridges during erection. J. Wind Eng. Ind. Aerodyn. **72**, 265–274 (1997)
3. Gunawan, L., Hadyan, H., Muhammad, H.: Measurements of flutter derivatives of a bridge deck sectional model. J. KONES **20**, 107–116 (2013)
4. Albano, L., William, P.R.: A doublet-lattice method for calculating lift distributions on oscillating surfaces in subsonic flows. AIAA J. **7**(2), 279–285 (1969)
5. Edwards, J.W., Bennett, R.M., Whitlow, W., Jr., Seidel, D.A.: Time-marching transonic flutter solutions including angle-of-attack effects. J. Aircr. **20**(11), 899–906 (1983)
6. Alonso, J., Antony J., Fully-implicit time-marching aeroelastic solutions. In: 32nd Aerospace Sciences Meeting and Exhibit (1994)
7. Prananta, B.B., Hounjet, M.H.L., Zwaan, R.J.: Two-dimensional transonic aeroelastic analysis using thin-layer Navier-Stokes method. J. Fluids Struct. **12**(6), 655–676 (1998)
8. Hall, K.C., Thomas, J.P., Dowell, E.H.: Proper orthogonal decomposition technique for transonic unsteady aerodynamic flows. AIAA J. **38**(10), 1853–1862 (2000)
9. Bohbot, J., Julien G., Stephane T., Denis D.: Computation of the flutter boundary of an airfoil with a parallel Navier-Stokes solver. In: 39th Aerospace Sciences Meeting and Exhibit, p. 572 (2001)
10. Tang, D., Dowell, E.H.: Experimental and theoretical study on aeroelastic response of high-aspect-ratio wings. AIAA J. **39**(8), 1430–1441 (2012)
11. Liu, F., Cai, J., Zhu, Y., Tsai, H.M., Wong, A.S.F.: Calculation of wing flutter by a coupled fluid-structure method. J. Aircr. **38**(2), 334–342 (2001)
12. Chen, X., Zha, G., Hu, Z., Yang, M.T.: Flutter prediction based on fully coupled fluid-structural interactions. In: 9th National Turbine Engine High Cycle Fatigue Conference (2004)
13. Badcock, K.J., Woodgate, M.A., Richards, B.E.: Direct aeroelastic bifurcation analysis of a symmetric wing based on the Euler equations. J. Aircr. **42**(3), 731–737 (2005)
14. Badcock, K.J., Woodgate, M.A.: Bifurcation prediction of large-order aeroelastic models. AIAA J. **48**(6), 1037–1046 (2010)
15. Badcock, K.J., Timme, S., Marques, S., Khodaparast, H., Prandina, M., Mottershead, J.E., Woodgate, M.A.: Transonic aeroelastic simulation for instability searches and uncertainty analysis. Prog. Aerosp. Sci. **47**(5), 392–423 (2011)
16. Timme, S., Marques, S., Badcock, K.J.: Transonic aeroelastic stability analysis using a Kriging-based Schur complement formulation. AIAA J. **49**(6), 1202–1213 (2011)
17. Wang, K. G., Beran, P. S., Cao, S.: Adjoint-based mesh adaptation for direct flutter prediction. In: International Forum on Aeroelasticity and Structural Dynamics (2017)
18. Frandsen, J., McRobie, F.A.: Finite element simulation of wind-induced bridge motion. In: Proceedings of the International Symposium on Computational Methods for Fluid-Structure Interaction, Cambridge (1999)
19. Schulz, K.W., Kallinderis, Y.: Unsteady flow structure interaction for incompressible flows using deformable hybrid grids. J. Comput. Phys. **143**, 569–597 (1998)
20. Larsen, A., Walther, J.H.: A two dimensional discrete vortex method for bridge aerodynamics applications. J. Wind Eng. Ind. Aerodyn. **67**, 183–193 (1997)

21. Morgenthal, G.: Aerodynamic analysis of structures using high-resolution vortex particle methods. Dissertation, University of Cambridge, Cambridge, United Kingdom (2002)
22. Koumoutsakos, P., Leonard, A.: High-resolution simulations of the flow around an impulsively started cylinder using vortex methods. J. Fluid Mech. **296**, 1–38 (1995)
23. Ploumhans, P., Winckelmans, G.S.: Vortex methods for high-resolution simulations of viscous flow past bluff bodies of general geometry. J. Comput. Phys. **165**(2), 354–406 (2000)
24. Ploumhans, P., Winckelmans, G.S., Salmon, J.K., Leonard, A., Warren, M.S.: Vortex methods for direct numerical simulation of three-dimensional bluff body flows: application to the sphere at Re= 300, 500, and 1000. J. Comput. Phys. **178**(2), 427–463 (2002)
25. Kamemoto, K.: On contribution of advanced vortex element methods toward virtual reality of unsteady vortical flows in the new generation of CFD. J. Braz. Soc. Mech. Sci. Eng. **26**(4), 368–378 (2004)
26. Cottet, G.-H., Poncet, P.: Advances in direct numerical simulations of 3D wall-bounded flows by vortex-in-cell methods. J. Comput. Phys. **193**(1), 136–158 (2004)
27. Yokota, R., Sheel, T.K., Obi, S.: Calculation of isotropic turbulence using a pure Lagrangian vortex method. J. Comput. Phys. **226**(2), 1589–1606 (2007)
28. Morgenthal, G., Walther, J.H.: An immersed interface method for the vortex-in-cell algorithm. Comput. Struct. **85**(11–14), 712–726 (2007)
29. Huang, M.J., Su, H.X., Chen, L.C.: A fast resurrected core-spreading vortex method with no-slip boundary conditions. J. Comput. Phys. **228**(6), 1916–1931 (2009)
30. Huang, C.J., Huang, M.J.: A vortex method suitable for long time simulations of flow over body of arbitrary geometry. Comput. Fluids **74**, 1–12 (2013)
31. Hammer, P., Altman, A., Eastep, F.: Validation of a discrete vortex method for low Reynolds number unsteady flows. AIAA J. **52**(3), 643–649 (2014)
32. Mimeau, C., Cottet, G.H., Mortazavi, I.: Direct numerical simulations of three-dimensional flows past obstacles with a vortex penalization method. Comput. Fluids **136**, 331–347 (2016)
33. Dung, D.V., Zuhal, L.R., Muhammad, H.: Two-dimensional fast Lagrangian vortex method for simulating flows around a moving boundary. J. Mech. Eng. **12**, 31–46 (2015)
34. Zuhal, L.R., Febrianto, E.V., Dung, D.V.: Flutter speed determination of two degree of freedom model using discrete vortex method. Appl. Mech. Mater. **660**, 639–643 (2014)
35. Greengard, L., Rokhlin, V.: A fast algorithm for particle simulations. J. Comput. Phys. **73**, 325–348 (1978)
36. Hrycak, T., Rokhlin, V.: An improved fast multipole algorithm for potential fields. SIAM J. Sci. Stat. Comput. **19**, 1804–1826 (1998)
37. Buard, R., Coutanceau, M.: The early stage of development of the wake behind an impulsively started cylinder for $40 < Re < 104$. J. Fluid Mech. **101**, 583–607 (1980)
38. Greengard, C.: The core-spreading vortex method approximations the wrong equation. J. Comput. Phys. **61**, 345–348 (1985)
39. Rossi, L.: Resurrecting core-spreading vortex methods: a new scheme that is both deterministic and convergent. SIAM J. Sci. Comput. **17**, 370–397 (1996)
40. Koumoutsakos, P., Leonard, A., Pepin, F.: Boundary conditions for viscous vortex methods. J. Comput. Phys. **113**, 52–61 (1994)
41. Nagao, F., Utsunomiya, H., Murata, S.: Improvement of pitching moment estimation of an oscillating body by discrete vortex method. J. Wind Eng. Ind. Aerodyn. **67**, 337–347 (1997)
42. Theodorsen, T., Mutchler, W.H.: General theory of aerodynamic instability and the mechanism of flutter. NACA Technical Report 496, United States (1935)
43. Walther, H.J., Larsen, A.: Two dimensional discrete vortex method for application to bluff body aerodynamics. J. Wind Eng. Ind. Aerodyn. **67**, 183–193 (1997)
44. Kim, Y.C.: Vortex-in-cell method combined with a boundary element method for incompressible viscous flow analysis. Int. J. Numer. Methods Fluids **69**, 1567–1583 (2011)
45. Taneda, S.: Studies on Wake Vortices (III). Experimental investigation of the wake behind a sphere at low Reynolds number. Rep. Res. Inst. Appl. Mech. **4**, 99–105 (1956)
46. Zhang, H.Q., Fey, U., Noack, B.R., König, M., Eckelmann, H.: On the transition of the cylinder wake. Phys. Fluids **7**(4), 779–794 (1995)
47. Barkley, D., Henderson, R.D.: Three-dimensional floquet stability analysis of the wake of a circular cylinder. J. Fluid Mech. **322**, 215–241 (1996)
48. Williamson, C.H.K.: The natural and forced formation of spot-like vortex dislocations in the transition of a wake. J. Fluid Mech. **243**, 393–441 (1992)
49. Thompson, M., Hourigan, K., Sheridan, J.: Three-dimensional instabilities in the wake of a circular cylinder. Exp. Thermal Fluid Sci. **12**(2), 190–196 (1996)
50. Rasmussen, J.T., Cottet, G.H., Walther, J.H.: A multiresolution remeshed vortex-in-cell algorithm using patches. J. Comput. Phys. **230**, 6742–6755 (2011)
51. Eldredge, J.D.: Numerical simulation of the fluid dynamics of 2D rigid body motion with the vortex particle method. J. Comput. Phys. **221**(2), 626–648 (2007)
52. Kinsey, T., Dumas, G.: Parametric study of an oscillating airfoil in a power-extraction regime. AIAA J. **46**(6), 1318–1330 (2008)
53. Ramesh, K., Gopalarathnam, A., Granlund, K., Ol, M., Edwards, J.: Discrete-vortex method with novel shedding criterion for unsteady aerofoil flows with intermittent leading-edge vortex shedding. J. Fluid Mech. **751**, 500 (2014)
54. Yu, M., Wang, Z.J., Hu, H.: High fidelity numerical simulation of airfoil thickness and kinematics effects on flapping airfoil propulsion. J. Fluids Struct. **42**, 166–186 (2013)